A scalar Poincaré map for anti-phase bursting in coupled inhibitory neurons with synaptic depression.

Mark Olenik [1,*], and Conor Houghton [2]

[1]School of Biological Sciences, Faculty of Life Sciences, University of Bristol, Bristol, United Kingdom
[2]School of Computer Science, Electrical and Electronic Engineering, and Engineering Mathematics, Faculty of Engineering, University of Bristol, Bristol, United Kingdom

Correspondence*:
Mark Olenik
m.olenik@bristol.ac.uk

2 ABSTRACT

Short-term synaptic plasticity is found in many areas of the central nervous system. In the inhibitory half-centre central pattern generators involved in locomotion, synaptic depression is believed to act as a burst termination mechanism, allowing networks to generate anti-phase bursting patterns of varying periods. To better understand burst generation in these central patter generators, we study a minimal network of two neurons coupled through depressing synapses. Depending on the strength of the synaptic conductance between the two neurons, this network can produce symmetric $n - n$ anti-phase bursts, where neurons fire n spikes in alternation, with the period of such solutions increasing with the strength of the synaptic conductance. Relying on the timescale disparity in the model, we reduce the eight-dimensional network equations to a fully-explicit scalar Poincaré burst map. This map tracks the state of synaptic depression from one burst to the next and captures the complex bursting dynamics of the network. Fixed points of this map are associated with stable burst solutions of the full network model, and are created through fold bifurcations of maps. We derive conditions that describe period-increment bifurcations between stable $n - n$ and $(n+1) - (n+1)$ bursts, producing a full bifurcation diagram of the burst cycle period. Predictions of the Poincaré map fit excellently with numerical simulations of the full network model and allow the study of parameter sensitivity for rhythm generation.

1 INTRODUCTION

Short-term synaptic plasticity may have a role in burst activity in central pattern generators (CPGs). Short-term synaptic depression is commonly found in neuronal networks involved in the generation of rhythmic movements, such as in the pyloric CPG of the spiny lobster [1, 2], or in the lumbosacral cord of the chick embryo [3]. Synaptic depression modulates the strength of synapses in response to changes to the presynaptic firing frequency. At a high neuronal firing frequency, depression weakens the strength of synapses and therefore reduces the magnitude of the postsynaptic response. At low firing frequency, it allows sufficient time for the synapse to recover from depression between spikes, leading to a stronger postsynaptic response. In reciprocal networks, synaptic depression has been shown to act as a "switch", giving rise to a wide range of network dynamics such as synchronous and multi-stable rhythms, as well as fine tuning the frequency of network oscillations [4, 5, 6].

Brown [7] pioneered the idea that synaptic depression acts as a burst termination mechanism in reciprocally inhibitory CPGs involved in rhythm generation of locomotion. When one side is firing during a burst the other, antagonistic side, is prevented from firing by synaptic inhibition. However, the weakening of inhibition as a result of synaptic depression eventually releases the antagonistic side so that it starts firing, terminating the burst on the side that had originally been firing. This rhythmogenesis hypothesis has been considered one of a handful of standard mechanisms for

37 generating locomotion rhythms in vertebrates [8, 9, 10]. It has been proposed as an explaination of
38 the antiphase burst rhythm in struggling in Xenopus tadpoles [11].

39 Bose and Booth [6] investigated burst generation in a generic half-centre CPG that consists of two
40 identical, tonically active Morris-Lecar [12] neurons coupled through inhibitory depressing synapses.
41 Numerical simulations showed that when the reciprocal synaptic conductance between the two
42 neurons is varied, the network produces symmetric $n - n$ anti-phase bursts, with stronger synaptic
43 coupling leading to longer bursts. They used methods from geometric singular perturbation theory
44 to separate the timescales of the fast membrane, and the slow synaptic dynamics of the network to
45 derive one-dimensional conditions necessary for the existence of stable $n - n$ solutions (for $n \leq 2$).
46 According to these conditions the type of firing pattern largely depends on the slow depression
47 dynamics of the synapses between the two neurons, and can therefore be predicted by knowing the
48 strengths of the synaptic conductances of the two synapses. Thus, the scalar conditions derived
49 in Bose and Booth [6] provide a method to numerically identify the type of stable $n - n$ pattern
50 for any given value of the coupling strength. However, they do not predict the exact period of
51 such solutions. Furthermore, while they provide good arguments for the validity of their reduction
52 assumptions and the resulting scalar conditions, they do not verify them numerically.

53 Here we extend the previous analysis by providing a Poincaré map of the slow depression dynamics.
54 This allows us not only to predict the types of stable $n - n$ solutions the full network can produce,
55 (for any n), but also to study how varying the coupling strength affects the period of such solutions.
56 To do this, we build on, and numerically test, the assumptions on the fast-slow timescale disparity
57 made in [6]. We reduce the two-cell model to a scalar Poincaré map that tracks the evolution of the
58 depression from the beginning of one burst to the beginning of the next burst. Stable fixed points of
59 our map are associated with stable $n - n$ burst solutions. Our map construction is motivated by the
60 burst length map of a T-type calcium current, utilised by Matveev et al. [13], which approximates
61 the anti-phase bursting dynamics of a network of two coupled Morris-Lecar neurons. In contrast to
62 our model, the network described in the [13] paper does not contain short-term synaptic depression,
63 and burst termination is instead accomplished through the dynamics of a slow T-type calcium
64 current.

65 The Poincaré map derived here replicates the results from numerical simulations of the full two-cell
66 ODE system: Given the strength of maximum conductance between the two neurons, fixed points of
67 our map predict the type and period of $n - n$ patterns, the switch between burst solutions of different
68 periods, as well as the occurrence of co-existent solutions. In addition to proving the existence and
69 stability of fixed points, our map shows that fixed points are created via a fold bifurcation of maps.
70 We also derive algebraic conditions that predict the period increment bifurcations that allow the
71 switch between $n - n$ and $(n + 1) - (n + 1)$ solutions. Because our map is fully explicit, it lays
72 the framework for studying the effects of other model parameter on network dynamics without the
73 need to run expensive numerical integrations of the ODEs.

74 This paper is organised as follows. First, we introduce the network of two neurons, and describe
75 the properties of single cell and synapse dynamics. We use numerical simulations of the network
76 to provide an intuition for the range of possible burst dynamics the system can produce. Next, we
77 state and justify the simplifying assumptions that are necessary for the map construction. Finally,
78 we analytically derive the first return map of the depression variable as well as the conditions that
79 are required for stable solutions to bifurcate between $n - n$ and $(n + 1) - (n + 1)$ solutions. We end
80 this work with a discussion.

2   MATERIALS AND METHODS

We consider a pair of identical Morris-Lecar neurons [12], with parameters adapted from [6]. The
Morris-Lecar model is a set of two first-order differential equations that describe the membrane
dynamics of a spiking neuron. The depolarisation is modelled by an instantaneous calcium current,
and the hyperpolarisation by a slow potassium current and a leak current. The membrane potential

v_i and potassium activation w_i of neuron i ($i, j = 1, 2$) is described by:

$$\dot{v}_i = f(v_i, w_i) - \bar{g}s_j(v_i - v_s), \tag{1}$$

$$\dot{w}_i = h(v_i, w_i). \tag{2}$$

Here v_s is the inhibitory reversal potential, and $\bar{g}$ and s_j are the maximal synaptic conductance and the synaptic gating, respectively, constituting the total inhibitory conductance $\bar{g}s_j$ from neuron j to neuron i. Function $f(v_i, w_i)$ describes the membrane currents of a single cell:

$$f(v_i, w_i) = -g_{\text{Ca}}m_\infty(v_i)(v_i - v_{\text{Ca}}) - g_{\text{K}}w_i(v_i - v_{\text{K}}) - g_{\text{L}}(v_i - v_{\text{L}}) + I. \tag{3}$$

The currents include a constant current I, and three ionic currents: an instantaneous calcium current, a potassium current, and a leak current, with respective reversal potentials v_{Ca}, v_{K}, and v_{L}, as well as maximum conductances g_{Ca}, g_{K}, and g_{L}. The function $h(v_i, w_i)$ models the kinetics of the potassium gating variable w_i, and is given by

$$h(v_i, w_i) = \frac{w_\infty(v_i) - w_i}{\tau_w} . \tag{4}$$

The steady-state activation functions m_∞ and w_∞ as well as the default model parameters are described in the Supplementary Material S1.

The dynamics of the synaptic interactions between the neurons are governed by a synaptic gating variable s_i and a depression variable d_i:

$$\dot{d}_i = \begin{cases} (1 - d_i)/\tau_a & \text{if } v_i < v_\theta, \tag{5} \\ -d_i/\tau_b & \text{if } v_i > v_\theta, \tag{6} \end{cases}$$

$$\dot{s}_i = \begin{cases} -s_i/\tau_\kappa & \text{if } v_i < v_\theta, \tag{7} \\ 0 & \text{if } v_i > v_{\theta.} \tag{8} \end{cases}$$

Variable d_i describes a firing rate dependent depletion mechanism that governs the amount of depression acting on the synapse. The model is agnostic with respect to the exact mechanism of this depletion, be it pre- or post-synaptic. When the voltage of cell i is above firing threshold ($v_i > v_\theta$), variable d_i decays with time constant τ_b, and recovers with time constant τ_a when voltage is below firing threshold ($v_i < v_\theta$). Since the synaptic inhibition occurs on a much faster timescale than synaptic depression, we assume that s_i is instantaneously reset to d_i whenever v_i increases above v_θ, where it remains throughout $v_i > v_\theta$. Whenever $v_i < v_\theta$, the synaptic variable decays exponentially with time constant τ_κ. The equations for the depression model were adapted from the Bose et al. [14] model. These equations are a mathematically tractable simplification of the established phenomenological depression model previously described by Tsodyks and Markram [15].

When the cells are uncoupled ($\bar{g} = 0$), the membrane dynamics are determined by the cubic v-nullcline $v_\infty(v_i)$ and the sigmoid w-nullcline $w_\infty(v_i)$, satisfying $\dot{v}_i = 0$ and $\dot{w}_i = 0$, respectively. The two curves intersect along the middle branch of v_∞, creating an unstable fixed point with a surrounding stable limit cycle of period $T = T_{act} + T_{inact}$ (fig. 1A). Here T_{act} is the amount of time the cell spends in the active state when $v > v_\theta$, while T_{inact} is the time it spends in the silent state when $v < v_\theta$. Trajectories along that limit cycle have the familiar shape of the action potential (fig. 1B). The trajectory of an action potential can be dissected into four phases: (1) a silent phase, (2) a jump up, (3) an active phase, and (4) a jump down [see e.g. 16]. During the silent phase the trajectory evolves along the left branch ($v_i < v_\theta$) of the cubic v-nullcline. Once the trajectory reaches the local minimum of v_∞, it "jumps up" to the right branch ($v_i > v_\theta$), crossing the firing threshold v_θ. During the active phase the trajectory then evolves along the right branch of the cubic until it arrives at the local maximum, where it "jumps down" to the left branch commencing a new cycle.

114   The two-cell network model is numerically integrated using an adaptive step-size integrator for
115   stiff differential equations implemented with XPPAUT [17] and controlled through the Python
116   packages SciPy [18] and PyXPP [19]. The following mathematical analysis is performed on the
117   equations of a single cell. Unless required for clarity, we will therefore omit the subscripts i, j from
118   here on.

3   RESULTS

3.1   Anti-phase burst solutions

120   Short-term synaptic depression of inhibition in a half-centre oscillator acts as a burst termination
121   mechanism [7] and is known to produce $n - n$ anti-phase burst solutions of varying period. Such
122   $n - n$ solutions consist of cells firing bursts of n spikes in alternation. Figure 2A shows the timecourse
123   of a typical $4 - 4$ burst. While one cell is firing a burst it provides an inhibitory conductance to
124   the other cell, preventing it from firing. Therefore, at any given moment one cell is spiking while
125   the other is inhibited. Consistent with Bose and Booth [6] we will refer to the currently firing cell
126   as "free" and we will call the inhibited cell "suppressed". Additionally, we will distinguish between
127   two phases of a $n - n$ solution: We will refer to the time interval when a cell is firing as the "free
128   phase", and we will call the remaining duration of a cycle, when a cell is not firing, the "suppressed
129   phase".

130   With each action potential of the free cell, short-term depression leads to a step-wise decrease
131   of d, and consequently of s (fig. 2B). If d depresses faster at spike time than it can recover in the
132   inter-spike-intervals (ISIs), the total synaptic conductance $\bar{g}s$ will eventually become sufficiently
133   small to allow for the suppressed cell to be released and start firing, thus inhibiting the previously
134   free cell. While a cell is suppressed its depression variable can recover. Once the suppressed cell
135   becomes free again its synaptic inhibition will be sufficient to terminate the burst of the previously
136   free cell and commence a new cycle. As previously demonstrated by Bose and Booth [6], in a two-
137   cell reciprocally inhibitory network with synaptic depression the coupling strength $\bar{g}$ determines
138   the type of $n - n$ solution. Increasing $\bar{g}$ produces higher $n - n$ burst solutions with more spikes
139   per burst and a longer cycle period. Figure 3 shows numerically stable $n - n$ solutions for varying
140   values of $\bar{g}$. For small values of $\bar{g}$ the network produces anti-phase spiking $1 - 1$ solutions. As $\bar{g}$ is
141   increased the network generates solutions of increasing n, that is $2 - 2$, $3 - 3$, and $4 - 4$. When $\bar{g}$ is
142   sufficiently large (bottom of fig. 3), one of the cells continuously spikes at its uncoupled period T
143   while the other cell remains fully suppressed. Depending on the initial conditions either of the two
144   cells can become the suppressed cell, which is why the suppressed solution is numerically bistable.

145   Branches of numerically stable $n - n$ solutions and their associated limit cycle period for varying
146   values of $\bar{g}$ are depicted in fig. 4A (see Supplementary Material S2 for algorithm description). Not
147   only do higher $n - n$ solutions branches require stronger coupling $\bar{g}$, but also within $n - n$ branches
148   the period increases with $\bar{g}$. In line with Bose and Booth [6] we find small overlaps between solution
149   branches indicating numerical bistability, for example such as between the $2 - 2$ and $3 - 3$ solution
150   branches. Branches of higher $n - n$ burst solutions occur on increasingly smaller intervals of $\bar{g}$, for
151   instance is the $\bar{g}$ interval of the $5 - 5$ branch shorter than that of the $4 - 4$ branch and so on.
152   The interval between the $5 - 5$ branch and the suppressed solution (region between dotted lines in
153   fig. 4A) not only contains even higher numerically stable $n - n$ solutions, such as $11 - 11$ bursts, but
154   also other non-symmetric $n - m$ solutions as well irregular, non-periodic solutions. However, the
155   analysis in the following sections will only be concerned with the numerically stable and symmetric
156   $n - n$ solutions.

3.2   Mathematical analysis of two-cell network

158   The goal of the following mathematical analysis is to reduce the complexity of the eight-
159   dimensional system to some easily tractable quantity. As we will see later this quantity is the
160   value of the depression variable d of either of the two cells. We will construct the solution of d in
161   a piecewise manner from one spike to the next, first during the free phase, and then during the
162   suppressed phase. This construction will require two assumptions about the membrane and synaptic
163   dynamics. The first assumption states that during a burst the free cell fires at its uncoupled period

164   T, which simplifies the construction of the solution of d. The second assumption states that once
165   the inhibitory conductance acting on the suppressed cell drops below a critical threshold, the
166   cell is immediately released and fires. The second assumption is necessary to predict the release
167   time of the suppressed cell, which allows us to model the recovery of d during the suppressed
168   phase. In other words, the second assumption requires that the release of the suppressed cell from
169   inhibition depends only on the timecourse of the inhibition, and not on the membrane dynamics
170   of the suppressed cell. Both assumptions can be observed in coupled relaxation-oscillator types
171   of neurons such as the Morris-Lecar model we use, and will be numerically verified below. Both
172   assumptions were first explored in [6] to derive algebraic conditions that guarantee the periodicity
173   of the depression variable for different $n - n$ solutions. However here we will use these assumptions
174   to construct a Poincaré map of d, which will provide a geometric intuition for the dynamics of the
175   full two-cell network and its dependence on model parameters.

176   Our first assumption about the model states that the free cell fires at its uncoupled period T,
177   that is, during the free phase of a burst we have $ISI = T$. Solution profiles in fig. 3 suggest that
178   the ISIs are indeed approximately constant. We can further numerically confirm this observation
179   by capturing the ISIs of the stable solutions from the bifurcation diagram in fig. 4A. In addition
180   to ISIs, Figure 4B also shows inter-burst intervals (IBIs), which correspond to the time interval
181   between the last spike of the burst and the full cycle period, and which lie in the suppressed phase
182   of the burst. IBIs lie on multiple branches, each branch associated with a stable $n - n$ solution,
183   and are monotonically increasing with $\bar{g}$. In contrast, ISIs are calculated from the spikes within the
184   free phase and do not vary significantly with $\bar{g}$, but are approximately $ISI \approx T$, affirming our first
185   assumption. Assuming $ISI = T$ allows us to ignore the non-linear membrane dynamics during the
186   free phase, and to construct the evolution of the synaptic variables iteratively from spike to spike.
187   Assuming $ISI = T$ seems reasonable given that inhibition acting on the suppressed cell decays
188   exponentially to zero on a much shorter timescale than the duration of the ISI, and therefore,
189   once the suppressed cell is released its trajectory quickly approaches the spiking limit cycle.

190   Our second assumption states that the suppressed cell is released and spikes as soon as the total
191   inhibitory conductance from the free cell drops below a constant threshold. We will now define
192   such a "release condition" by exploiting the discrepancy in timescales between the fast membrane
193   dynamics, and the slower synaptic dynamics. Let us first consider the dynamics of a single Morris-
194   Lecar neuron. We fix the synaptic variable that acts on the cell by setting $s = 1$, which also makes
195   the applied synaptic conductance $\bar{g}s$ constant. Recall from fig. 1A that in case of a single uncoupled
196   cell ($\bar{g}s = 0$), the v- and w-nullclines intersect at some unstable fixed point $p_f = (v_f, w_f)$, while
197   trajectories revolve around a stable spiking limit cycle. Increasing $\bar{g}s$ moves the cubic v_∞ with the
198   ensuing unstable fixed point p_f down the sigmoid w_∞ in the $(v - w)$-plane (fig. 5). When $\bar{g}s$ is large
199   enough, the fixed point p_f becomes stable, attracting all previously periodic trajectories. There
200   exists a unique value $\bar{g}s = g^\star$ when p_f changes stability and the stable limit cycle vanishes. Thus,
201   when a constant inhibitory conductance is applied, $\bar{g}s < g^\star$ acts as a necessary condition for a cell
202   to spike. In contrast, when $\bar{g}s > g^\star$ inhibition is strong enough to prevent a cell from spiking [6].

203   Now let us analyse the nullclines of the suppressed cell when the two cells are coupled via synaptic
204   inhibition with depression. Let $\bar{g}s$ here denote the total synaptic conductance which acts on the
205   suppressed cell and is produced by the free cell, and let p_f be the fixed point associated with the
206   suppressed cell. At the start of the burst of the free cell we have $\bar{g}s > g^\star$ and p_f is stable. When
207   the free cell spikes, $\bar{g}s$ peaks (??), and the v-nullcline with the ensuing stable p_f move down the
208   w-nullcline. Then in between spikes $\bar{g}s$ decays exponentially (??) causing the v-nullcline and p_f to
209   move up the w-nullcline while attracting trajectories of the suppressed cell. Once depression causes
210   the synaptic conductance to become small enough to satisfy $\bar{g}s < g^\star$ and the suppressed cell is
211   released, fixed point p_f becomes unstable allowing the suppressed cell to fire. If the trajectory of
212   the suppressed cell remains sufficiently close to the stable p_f at the time when it changes stability,
213   then $\bar{g}s < g^\star$ acts as a release condition that is not only necessary, but also sufficient for firing of
214   the suppressed cell. In this case the release of the suppressed cell occurs precisely when

$$\bar{g}s = g^\star \tag{9}$$

215   is satisfied.

216   Whether the (v, w)-trajectory of the suppressed cell can remain close enough to p_f to make eq. (9)
217   sufficient for firing depends largely on the coupling strength $\bar{g}$ and the timescale disparity between
218   membrane dynamics and synaptic dynamics [6]. It is straightforward to test our assumption of
219   a release condition by numerically integrating the full system of ODEs and calculating the time
220   interval between the first spike of the suppressed cell and the time when $\bar{g}s$ first crosses $g^\star$. We will
221   call this time interval the "release delay". If our assumption holds, we would expect an approximately
222   zero release delay. Figure 6 shows the numerically computed graph of the release delay for varying
223   $\bar{g}$. The graph shows three distinct branches, next to each branch we also plot the timecourse of a
224   corresponding sample solution of the total synaptic conductance $\bar{g}s$ of both cells. For the rightmost
225   branch where $\bar{g} > 0.592$ mS/cm^2 the release delay is approximately zero. Here the first spike of the
226   suppressed cell can be accurately predicted by the release condition in eq. (9). The leftmost and
227   middle branches for $\bar{g} < 0.592$ mS/cm^2 show a release delay greater than zero, the suppressed cell
228   does not immediately fire when the release condition is first satisfied, and eq. (9) does not accurately
229   predict the release of the suppressed cell. The leftmost and middle branches contain $1 - 1$ and $2 - 2$
230   solutions respectively. In both cases the coupling $\bar{g}$ is not sufficiently strong to allow trajectories of
231   the suppressed cell to be close enough to p_f to guarantee spiking once $\bar{g}$ crosses $g^\star$. Note that in the
232   middle branch $\bar{g}s$ crosses $g^\star$ twice, and only after the second crossing does the suppressed cell fire.
233   The following map construction relies on the assumption that the release condition in eq. (9) can
234   accurately predict the release time of the suppressed cell. Given our model parameters this is only
235   possible for sufficiently large $\bar{g} > 0.592$ mS/cm^2. For completeness, however, we will also consider
236   values $\bar{g} < 0.592$ mS/cm^2 in the following analysis, bearing in mind that in this parameter range
237   our map will not be accurate.

238   In summary: For $\bar{g} > 0.592$ mS/cm^2 the release condition is sufficient to predict when the
239   suppressed cell is released. Due to the symmetry of $n - n$ solutions the release occurs at exactly half
240   the period of the full cycle, that is at $P/2$. The release time therefore uniquely determines the type
241   of $n - n$ solution. Furthermore, computation of the release time does not depend on the membrane
242   nor the synaptic dynamics of the suppressed cell. Instead, the solution of the synaptic variable s
243   of the free cell is sufficient to predict when $\bar{g}s = g^*$ is satisfied. Finally, s is solely determined by
244   the evolution of the depression variable d of the free cell. Constructing a solution of d during the
245   free phase of either cell will therefore uniquely determine the solution of the full eight-dimensional
246   network. However, finding the solution d requires us to know the initial value $d(0)$ at the start of
247   a cycle at $t = 0$. In the next section we will construct a scalar return map that tracks these initial
248   values $d(0)$ from cycle to cycle of stable $n - n$ solutions.

249   3.3   Construction of the scalar Poincaré map

250   In this section we construct the scalar Poincaré map $\Pi_n : d^\star \mapsto d^\star$. Here the discrete variable $d^\star$
251   tracks the values of the continuous depression variable d at the beginning of each $n - n$ burst. The
252   map Π_n therefore describes the evolution of d, of either of the two cells, from the beginning of one
253   cycle to the beginning of the next cycle. To simplify the map construction we will assume that a
254   free cell fires exactly n times before it becomes suppressed. We will construct Π_n by evolving d first
255   during the free phase and then during the suppressed phase of the $n - n$ limit cycle. First, let us
256   give explicit definitions of the free and suppressed phases. A schematic illustration of both phases
257   is given in fig. 7.

258   Suppose that at $t = 0$ cell 1 starts free with some initial $d(0)$. Cell 1 then fires n spikes at
259   the uncoupled period $T = T_{act} + T_{inact}$. Let $s(t)$ and $d(t)$ be the corresponding solutions of the
260   synaptic and depression variables of cell 1. After n spikes the total conductance $\bar{g}s(t)$ acting on
261   the suppressed cell 2 has decayed sufficiently to satisfy the release condition (9). That is at some
262   time $t = (n - 1)T + T_{act} + \Delta t$, where $\Delta t < T_{inact}$, we have $\bar{g}s(t) = g^\star$. Cell 2 is then released and
263   prevents cell 1 from further spiking. Here Δt is the time between the last spike of cell 1 and the
264   first spike of cell 2 [6]. Once released, cell 2 also fires n spikes until cell 1 becomes free once again.
265   Let P_n denote the full cycle period of a $n - n$ solution:

$$P_n = 2\Big((n-1)T + T_{act} + \Delta t\Big). \tag{10}$$

266 We can now define the free and suppressed phases of cell 1 explicitly. The free phase is the interval
267 that lasts from the first spike time up until the beginning of the inactive phase of the last spike,
268 last spikes of the burst, that is for time $0 < t < (n-1)T + T_{act}$. During the free phase of cell 1,
269 the suppressed cell 2 is inhibited sufficiently strong to prevent it from firing, hence $\bar{g}s > g^\star$. The
270 suppressed phase of cell 1 is the remaining duration of the cycle when the cell is not firing, that is
271 for $(n-1)T + T_{act} < t < P_n$. Hence the suppressed phase lasts for $(n-1)T + T_{act} + 2\Delta t$.

272   Note that only the suppressed phase depends on Δt, which will play a central role in the
273 construction of Π_n. From eq. (10) Δt can be computed as

$$\Delta t = \frac{1}{2}P_n - (n-1)T - T_{act}. \tag{11}$$

274 We can use eq. (11) and the numerically computed bifurcation diagram of the period for stable $n-n$
275 solutions in fig. 4A to obtain the graph of Δt as a function of $\bar{g}$ (fig. 8). Each continuous branch of
276 Δt is monotonically increasing and corresponds to a $n-n$ burst: Stronger coupling $\bar{g}$ increases the
277 total synaptic conductance $\bar{g}s$ that acts on the suppressed cell, thus delaying its release. It is easy
278 to see that for any n-branch we have $\Delta t < T_{inact}$: Once Δt crosses T_{inact}, the free cell can "squeeze
279 in" an additional spike and the solutions bifurcate into a $(n+1)-(n+1)$ burst.

280   Distinguishing between the free and suppressed phases of a cycle allows us to describe the
281 dynamics of the depression variable d explicitly for each phase. As can be seen from fig. 7C,
282 during the free phase d depresses when $v > v_\theta$ and recovers when $v < v_\theta$. In contrast, during the
283 suppressed phase d only recovers and does not depress. Given the initial $d^\star = d(0)$ at the beginning
284 of the cycle and the number of spikes in the free phase n, we can now construct the burst map Π_n.
285 The map

$$\Pi_n(d^\star) = Q_n\big(F_n(d^\star)\big) \tag{12}$$

286 is a composition of two maps. Map

$$F_n : d^\star \mapsto \Delta t \tag{13}$$

287 models the evolution of d in the free phase. F_n takes an initial value $d^\star$ and calculates Δt. Map

$$Q_n : \Delta t \mapsto d^\star \tag{14}$$

288 models the recovery of d in the suppressed phase. Given some Δt map Q_n computes $d^\star$ at the start
289 of the next cycle.

290   Our aim in the following analysis is to elucidate the properties of Π_n and to understand the
291 structure of its parameter space by exploring how the stable and unstable fixed points of Π_n are
292 created. To that effect it will be useful to include not only positive, but also negative values of $d^\star$
293 to the domain of Π_n. But it is important to add that values $d^\star < 0$ are biologically impossible as
294 the depression variable models a finite pool of neurotransmitters, and therefore must be positive.
295 Because Π_n maps first from $d^\star$ to Δt, and then back to $d^\star$, we will also consider negative values of
296 Δt, interpreting them as $n-n$ solutions with partially overlapping bursts. As will become evident,
297 $\Delta t < 0$ is only a formal violation of the biological realism of the map Π_n, as numerically stable
298 $n-n$ solutions of the full system of ODEs only exist for $\Delta t > 0$.

299   We start the construction of Π_n by first considering the free phase and building the map F_n. At
300 each spike time t_k where $d(t_k) = d_k$, variable d decays first for the duration of the active phase of
301 the spike for T_{act}, as described by the solution to ??. At $t = t_k + T_{act}$ we have

$$d(t_k + T_{act}) = d_k e^{-T_{act}/\tau_b}. \tag{15}$$

302 The depression variable then recovers during the inactive phase of the spike until t_{k+1}, where for
303 $0 < t < T_{inact}$:

$$d(t_{k+1}) = 1 - (1 - d_k e^{-T_{act}/\tau_b})e^{-t/\tau_a}. \tag{16}$$

304 By substituting $t = T_{inact}$ we can build a linear map that models the depression of d from spike
305 time t_k to the subsequent spike time t_{k+1} during the free phase:

$$d_{k+1} = \lambda\rho d_k + (1 - \rho), \tag{17}$$

where to keep the notation simple we let

$$\lambda := \exp(-T_{act}/\tau_b), \tag{18}$$

$$\rho := \exp(-T_{inact}/\tau_a). \tag{19}$$

306   Given constant T_{act} and T_{inact}, parameter λ determines how much the synapses depresses during
307   the active phase of the spike, while ρ determines how much it recovers during the inactive phase.
308   Since $0 < \lambda, \rho < 1$, map eq. (17) is increasing and contracting, with a fixed point at

$$d_s = \frac{1 - \rho}{1 - \lambda\rho}, \tag{20}$$

309   where $0 < d_s < 1$. The value d_s is the maximum depression value that can be observed in the
310   suppressed solution where the active cell fires at its uncoupled period T (see fig. 3E). Using the
311   release condition in eq. (9) allows us to derive the value of the minimum coupling strength that will
312   produce the full suppressed solution, denoted as $\bar{g}_s$. Solving ?? for $s(t)$ with $t = T_{inact}$ and setting
313   the initial value $s(0) = d_s\lambda$ gives

$$\bar{g}_s d_s \lambda e^{-T_{inact}/\tau_\kappa} = g^\star. \tag{21}$$

314   By further substituting the definition of d_s in (20) and rearranging, we can write $\bar{g}_s$ as a function
315   of λ and ρ:

$$\bar{g}_s(\lambda, \rho) = \frac{1/\lambda - \rho}{1 - \rho} e^{T_{inact}/\tau_\kappa} g^\star. \tag{22}$$

316   Note that the above dependence of $\bar{g}_s$ on λ is linear and monotonically decreasing. Increasing λ
317   reduces the strength of the depression of the free cell. This in turn allows the free cell to fully
318   suppress the suppressed cell at smaller values of $\bar{g}$.

319   Solving eq. (17) gives us the linear map $\delta_n : d^\star \mapsto d_n$, that for some initial $d^\star$ computes the
320   depression at the nth spike time, $d_n = d(t_n)$:

$$\delta_n(d^\star) = (\lambda\rho)^{n-1} d^\star + (1 - \rho) \sum_{i=0}^{n-2} (\lambda\rho)^i. \tag{23}$$

321   Since $\lambda < 1$, function δ_n is a linearly increasing function of $d^\star$ with a fixed point at d_s for all n.
322   Having identified d after n spikes, we can now use the release condition $\bar{g}s = g^\star$ (eq. (9)) to find
323   Δt. At the last (nth) spike of the free phase at time $t_n = (n-1)T$ the synapse variable s is set to
324   the respective value of $d(t_n) = \delta_n(d^\star)$, and mirrors the value of d for the duration of T_{act}. at the
325   end of the active phase at time $t_n + T_{act}$ variable d has decayed to $\delta_n(d^\star)\lambda$ eq. (18), therefore

$$s(t_n + T_{act}) = \delta_n(d^\star)\lambda. \tag{24}$$

326   Finally s decays exponentially for $\Delta t < T_{inact}$. Solving ?? (case $v < v_\theta$) with initial condition
327   $s(0) = \delta_n(d^\star)\lambda$ yields:

$$s(\Delta t) = \delta_n(d^\star)\lambda e^{-\Delta t/\tau_\kappa}. \tag{25}$$

328   Substituting $s(\Delta t)$ into s of the release condition (eq. (9)) gives then

$$\bar{g}\delta_n(d^\star)\lambda e^{-\Delta t/\tau_\kappa} = g^\star. \tag{26}$$

329   Our assumption of the release condition guarantees that the suppressed cell 2 spikes and becomes
330   free when $\bar{g}s - g^\star$ crosses zero. Solving eq. (26) for Δt allows us to compute it a function of $d^\star$,
331   which defines our map F_n:

$$F_n(d^\star) := \tau_\kappa \ln\left(\frac{\bar{g}}{g^\star}\lambda\delta_n(d^\star)\right) = \Delta t. \tag{27}$$

332   Figure 9A shows F_n for various n, which is a strict monotonically increasing function of $d^\star$ as
333   well as $\bar{g}$. Larger values of $d^\star$ and $\bar{g}$, respectively, cause stronger inhibition of the suppressed cell,

334 and therefore prolong its release time and the associated Δt. Map F_n is defined on $d^\star > d_a$, where
335 d_a is a vertical asymptote found by solving $\delta_n(d^\star) = 0$ in eq. (23) for $d^\star$, which yields

$$d_a(n) = -\frac{(1-\rho)\sum_{i=0}^{n-2}(\lambda\rho)^i}{(\lambda\rho)^{n-1}} \le 0 \ . \tag{28}$$

336 We now turn to the construction of map Q_n, which describes the recovery of the depression
337 variable during the suppressed phase. As we have identified earlier, the recovery in the suppressed
338 phase of a $n-n$ solution is of duration $(n-1)T + T_{act} + 2\Delta t$. Substituting that into the solution
339 of d (??) with the initial condition $d(0) = \delta_n(d^\star)\lambda$ yields the map Q_n:

$$Q_n(\Delta t) := 1 - (1 - \delta_n(d^\star)\lambda)e^{-((n-1)T+T_{act}+2\Delta t)/\tau_a}. \tag{29}$$

340 Given Δt, we can find $\delta_n(d^\star)$ by rearranging the release condition in eq. (26):

$$\delta_n(d^\star) = \frac{1}{\bar{g}\lambda}g^\star e^{\Delta t/\tau_\kappa}. \tag{30}$$

341 Map Q_n is shown in fig. 9B for various values n. Note that Q_n is monotonically increasing as larger
342 values Δt imply a longer recovery time, and hence Q_n grows without bound. All curves Q_n intersect
343 at some $\Delta t = \tau_\kappa \ln[\bar{g}/g^\star]$ where

$$Q_n\left[\tau_\kappa \ln\left(\frac{\bar{g}}{g^\star}\right)\right] = 1. \tag{31}$$

344 As we will show in the next section, all fixed points of the full map Π_n occur for $d^\star < 1$. We
345 will therefore restrict the domain of Q_n to $(-\infty, \tau_\kappa \ln[\bar{g}/(g^\star)])$ and the codomain to $(-\infty, 1)$.
346 Additionally, while values $\Delta t > T$ will be helpful in exploring the geometry of Π_n, recall from fig. 8
347 that in the flow system all $n-n$ solutions bifurcate into $(n+1)-(n+1)$ solutions exactly when
348 $\Delta t = T_{inact}$, and we will address this concern in the last part of our map analysis.

349 Having found F_n and Q_n, we can now construct the full map $\Pi_n(d^\star) = Q_n\big(F_n(d^\star)\big)$:

$$\Pi_n(d^\star) = 1 - \left(1 - \delta_n(d^\star)\lambda\right)\left(\frac{\bar{g}}{g^\star}\delta_n(d^\star)\lambda\right)^{-\tau}e^{-((n-1)T+T_{act})/\tau_a}, \tag{32}$$

350 where we substituted $\tau = 2\tau_k/\tau_a$. Since d is the slowest variable of the system and $\tau_a \gg \tau_\kappa$, we will
351 also assume $\tau < 1$. Figure 10A depicts Π_n for various n. Intersections of Π_n with the diagonal are
352 fixed points of the map. Figure 10B shows Π_2 with $n = 2$. Varying the synaptic strength $\bar{g}$ moves
353 the curves Π_n up and down the $(d^\star, \Pi_n)$-plane. For $\bar{g} < 0.03$ mS/cm^2 map Π_2 has no fixed points.
354 As $\bar{g}$ is increased to $\bar{g} \approx 0.03$ mS/cm^2, curve Π_2 coalesces with the diagonal tangentially. When
355 $\bar{g} > 0.03$ mS/cm^2, a pair of fixed points emerge, one stable and one unstable fixed point, indicating
356 the occurrence of a fold bifurcation of maps.

From eq. (32) it is evident that Π_n is monotonically increasing with respect to $\bar{g}$ and also $d^\star$:

$$\frac{d\Pi_n}{d\bar{g}} > 0, \tag{33}$$

$$\frac{d\Pi_n}{dd^\star} > 0, \tag{34}$$

357 and in the following sections we will heavily rely on this monotonicity property of Π_n. Just as F_n,
358 curves Π_n spawn at the asymptote d_a (eq. (28)), and because

$$\lim_{\bar{g}\to\infty}\Pi_n = 1 \text{ for all } n, \tag{35}$$

359 fixed points of Π_n lie in $(d_a, 1)$.

360 ### 3.4 Existence and stability of fixed points

361 We introduce the fixed point notation $d_f^\star$ with $\Pi_n(d_f^\star) = d_f^\star$. The existence of fixed points $d_f^\star$
362 for $\bar{g}$ sufficiently large can be shown from the strict monotonicity of Π_n with respect to $\bar{g}$ and $d^\star$
363 (eqs. (33) and (34)), as well as the fact that the slope of Π_n is monotonically decreasing,

$$\left(\frac{\mathrm{d}}{\mathrm{d}d^\star}\right)^2 \Pi_n < 0. \tag{36}$$

In the limit $d^\star \to d_a$ the value of Π_n decreases without bound for any $\bar{g} > 0$. In the limit $\bar{g} \to 0$, Π_n
also decreases without bound, but as $\bar{g} \to \infty$ values of Π_n approach 1. It follows from eq. (33) and
the intermediate value theorem that for some $\bar{g}$ large enough Π_n intersects the diagonal. Moreover,
because Π_n and its slope are monotonic with respect to $d^\star$, there exists some critical fixed point
$(d_b^\star, \bar{g}_b)$ where Π_n aligns with the diagonal tangentially with

$$\Pi_n(d_b^\star, \bar{g}_b) = d_b^\star, \tag{37}$$

$$\frac{d}{d^\star}\Pi_n(d_b^\star, \bar{g}_b) = 1. \tag{38}$$

364 Equations (33) and (36) constitute the non-degeneracy conditions for a codimension-1 fold
365 bifurcation of maps, indicating that in a neighbourhood of $(d_b^\star, \bar{g}_b)$ map Π_n has the topological
366 normal form described by the graph of

$$x \mapsto \beta + x - x^2, \tag{39}$$

367 with a stable and unstable fixed point $x = \pm\sqrt{\beta}$, and slopes $\mathrm{d}x/\mathrm{d}\beta = \mp(2\sqrt{\beta})^{-1}$, respectively.

368 ### 3.5 Fold bifurcations of maps

369 Fixed points of Π_n satisfy the fixed point equation

$$\Phi_n(d^\star, \bar{g}) := \Pi_n(d^\star, \bar{g}) - d^\star = 0. \tag{40}$$

370 As we have already shown, for $\bar{g} > \bar{g}_b(n)$ solutions to eq. (40) exist in pairs of stable and unstable
371 fixed points. Solving eq. (40) explicitly for $d^\star$ it not trivial, but solving for $\bar{g}$ is straightforward and
372 given by $\bar{g} = G_n(d^\star)$, where

$$G_n(d^\star) := \frac{g^\star}{\delta_n(d^\star)\lambda}\left(\frac{(1 - \lambda\delta_n(d^\star))}{1 - d^\star}e^{-((n-1)T+T_{act})/\tau_a}\right)^{1/\tau}. \tag{41}$$

373 Plotting $d^\star$ against $\bar{g}$ gives the fixed point curves, which are shown in fig. 11A. Note the typical
374 quadratic shape of a fold bifurcation of maps. It is also evident that the fold bifurcations occur for
375 increasingly smaller $\bar{g}$ as n is increased. Moreover, we can observe that unstable fixed points have
376 negative values of $d^\star$ for $n > 1$.

Equation (41) also allows us to find the critical fixed point connected with the fold bifurcation,
namely $\left(d_b^\star(n), \bar{g}_b(n)\right)$, which is the global minimum of $G_n(d_f^\star)$:

$$d_b^\star(n) = \operatorname{argmin} G_n(d_f^\star), \tag{42}$$

$$\bar{g}_b(n) = \min G_n(d_f^\star). \tag{43}$$

Function G_n is strictly monotonic on the respective intervals of $d_f^\star$ that correspond to the stable
and unstable fixed points, that is

$$\frac{\mathrm{d}G_n}{\mathrm{d}d_f^\star} < 0, \text{ for } d_f^\star > d_b^\star(n) \text{ stable}, \tag{44}$$

$$\frac{\mathrm{d}G_n}{\mathrm{d}d_f^\star} > 0, \text{ for } d_f^\star < d_b^\star(n) \text{ unstable}, \tag{45}$$

377 which allows us to express the stable and unstable fixed points as the inverse of G_n on their
378 respective intervals of $d_f^\star$. Because we are primarily interested in the stable fixed points, we define
379 the stable fixed point function $d_f^\star = \phi_n(\bar{g})$ as

$$\phi_n(\bar{g}) := G_n^{-1}(d_f^\star) \text{ for } d_f^\star > d_b^\star(n). \tag{46}$$

380 Function $\phi_n(\bar{g})$ is also monotonic, and is therefore straightforward to compute numerically. Here
381 we use the Python package Pynverse [20] for that purpose.

382   Having found the stable fixed points $d_f^\star$ as a function of $\bar{g}$, we can now compute the associated
383 cycle period. Recall that the period is given by eq. (10), which we can be written as a function of
384 $\bar{g}$:

$$P_n(\bar{g}) = 2\Big((n-1)T + T_{act} + F_n\big(\underbrace{\phi_n(\bar{g})}_{d_f^\star}, \bar{g}\big)\Big), \tag{47}$$

385 where map F_n (eq. (27)) calculates Δt given a stable fixed point $d_f^\star = \phi_n(\bar{g})$. We plot the predicted
386 period $P_n(\bar{g})$ versus the cycle period that was computed from numerically integrating the full system
387 of ODEs in fig. 11B. For $n > 1$ our map Π_n accurately predicts the period. When laying out our
388 assumptions in section 3.2, we have already predicted an inaccuracy for $n = 1$ (see fig. 6), since
389 here $\bar{g}$ is not sufficiently strong to guarantee the validity of our release condition (eq. (9)).

390   It is evident from fig. 11A that ϕ_n is strictly increasing with $\bar{g}$. This property follows directly
391 from the normal form of the fold bifurcation (eq. (39)), but can also be shown using implicit
392 differentiation and the fixed point equation $\Phi_n(\phi_n(\bar{g}), \bar{g}) = 0$ in eq. (40). For $d_f^\star = \phi_n(\bar{g}) > d_b(n)$
393 we get:

$$\frac{\mathrm{d}\phi_n}{\mathrm{d}\bar{g}} = -\frac{\partial\Phi_n/\partial\bar{g}}{\partial\Phi_n/\partial d^\star} = \frac{\partial\Pi_n/\partial\bar{g}}{1 - \partial\Pi_n/\partial d^\star} > 0. \tag{48}$$

394 The inequality follows from $\partial\Pi_n/\partial\bar{g} > 0$ and the fact that $\partial\Pi_n/\partial d^\star < 1$ for $d^\star > d_b(n)$. ?? allows
395 us to explain why the period P_n increases with $\bar{g}$, as seen in fig. 11B. Differentiating P_n gives:

$$\frac{\mathrm{d}P_n}{\mathrm{d}\bar{g}} = 2\boldsymbol{\nabla}F_n(d_f^\star, \bar{g}) \cdot \begin{bmatrix} \partial\phi_n/\partial\bar{g} \\ 1 \end{bmatrix} > 0, \tag{49}$$

where the partial derivatives of $F_n(d_f^\star, \bar{g})$ are:

$$\frac{\partial F_n}{\partial d_f^\star} = \tau_s \frac{(\lambda\rho)^{n-1}}{\delta_n(d_f^\star)} > 0, \tag{50}$$

$$\frac{\partial F_n}{\partial\bar{g}} = \frac{\tau_s}{\bar{g}} > 0. \tag{51}$$

396 ?? and eq. (49) have an intuitive biological interpretation: Increasing the coupling strength between
397 the neurons leads to overall stronger inhibition of the suppressed cell, which delays its release and
398 leads to a longer cycle period. The latter allows more time for the synapse to depress in the free
399 phase and recover in the suppressed phase, resulting in overall larger values of $d_f^\star$, that is weaker
400 depression at the burst onset.

401   While fixed points of our Poincaré map predict the cycle period of the flow system excellently,
402 its construction relies on the strong assumption that the free phase contains exactly n spikes. As
403 is evident from fig. 11B this assumption is clearly violated in the flow system, as stable $n - n$
404 bursts exists only on certain parameter intervals of $\bar{g}$. In the last sub-section we will analyse the
405 mechanisms that guide how the stable $n - n$ are created and destroyed, and use our previous
406 analysis to derive the corresponding parameter intervals of $\bar{g}$ where such solutions exist.

407   ## 3.6   Period increment bifurcations with co-existent attractors

Let $\bar{g}_+(n)$ and $\bar{g}_-(n)$ denote the left and right parameter borders on $\bar{g}$ where stable $n-n$ solutions exist. That is, as $\bar{g}$ is increased stable $n-n$ solutions are created at $\bar{g}_+(n)$ and destroyed at $\bar{g}_-(n)$. When $\bar{g}$ is reduced beyond $\bar{g}_+(n)$, $n-n$ solutions bifurcate into $(n-1)-(n-1)$ solutions, while when $\bar{g}$ is increased beyond $\bar{g}_-(n)$, $n-n$ solutions bifurcate into $(n+1)-(n+1)$ solutions. Let us briefly recap our observations regarding $\bar{g}_+(n)$ and $\bar{g}_-(n)$ from the numerical bifurcation diagram in fig. 11B. For $n > 1$ there are the following relations:

$$\bar{g}_+(n) < \bar{g}_-(n), \tag{52}$$

$$\bar{g}_+(n) < \bar{g}_+(n+1) \text{ and } \bar{g}_-(n) < \bar{g}_-(n+1), \tag{53}$$

$$\bar{g}_+(n+1) < \bar{g}_-(n), \tag{54}$$

$$\bar{g}_-(n+1) - \bar{g}_+(n+1) < \bar{g}_-(n) - \bar{g}_-(n). \tag{55}$$

408   Equations (52) and (53) are self-explanatory. Equation (54) formally describes occurrence of co-
409   existence between stable $n-n$ and $(n+1)-(n+1)$ solutions. Equation (55) implies that the
410   parameter interval on $\bar{g}$ of $n-n$ solutions decreases with n, in other words, bursts with more
411   spikes occur on increasingly smaller intervals of the coupling strength. All of the above relations
412   are reminiscent of the period increment bifurcations with co-existent attractors, first described
413   for piecewise-linear scalar maps with a single discontinuity by Avrutin and colleagues [e.g. see
414   21, 22, 23, 21]. While our maps Π_n are fully continuous, the above observation suggests that a
415   different piecewise-linear scalar map that captures the period increment bifurcations of the full
416   system might exist. We will explore what such a map might look like in the discussion.

417   Let us now find algebraic equations that will allow us to calculate the critical parameters $\bar{g}_+(n)$
418   and $\bar{g}_-(n)$ associated with the period increment bifurcations. Recall that the period P_n derived
419   from the fixed points of Π_n is an increasing function of $\bar{g}$:

$$\frac{\mathrm{d}P_n}{\mathrm{d}\bar{g}} = 2\frac{\mathrm{d}F_n(\phi_n(\bar{g}),\bar{g})}{\mathrm{d}\bar{g}} > 0, \tag{56}$$

420   that is, as the coupling strength increases, it takes longer for the total synaptic conductance to
421   fall below the value of the release conductance, which delays the release of the suppressed cell, and
422   Δt becomes larger. When $\Delta t > T_{inact}$, the free cell can produce another spike and the solution
423   bifurcates into a $(n+1)-(n+1)$ solution. Note, however, that at $\bar{g}_+(n)$ the bifurcation into a
424   $(n-1)-(n-1)$ does not occur at $\Delta t = 0$. Here the mechanism is different: A sufficient reduction
425   of $\bar{g}$ causes the total synaptic conductance to drop below the release conductance in the previous
426   ISI, which allows the suppressed cell to be released one spike earlier.

427   Using the above reasoning we can now formulate the conditions for both bifurcations at $\bar{g}_+(n)$
428   and $\bar{g}_-(n)$. As in the previous sections, we will only restrict ourselves to the analysis of the stable
429   fixed points given implicitly by $d_f^\star = \phi_n(\bar{g})$ (eq. (46)). At the right bifurcation border $\bar{g}_-(n)$ we
430   have $\Delta t = T_{inact}$, and after substituting our F_n map (eq. (27)) this translates into

$$F_n(\phi_n(\bar{g}),\bar{g}) = T_{inact}, \tag{57}$$

431   which lets us define a function

$$\mathcal{R}_n(\bar{g}) := F_n(\phi_n(\bar{g}),\bar{g}) - T_{inact}, \tag{58}$$

432   whose root is the desired right bifurcation border $\bar{g}_-(n)$. In case of the left bifurcation border at
433   $\bar{g}_+(n)$, the release condition is satisfied just before the free cell has produced its nth spike, where
434   total synaptic conductance is given by

$$\bar{g}\delta_{n-1}\big(\phi_n(\bar{g})\big)\lambda e^{-T_{inact}/\tau_\kappa} = g^\star, \tag{59}$$

435   which can be rewritten as a function

$$\mathcal{L}_n(\bar{g}) := \bar{g}\delta_{n-1}\big(\phi_n(\bar{g})\big)\lambda e^{-T_{inact}/\tau_\kappa} - g^\star, \tag{60}$$

436   whose root is $\bar{g}_+(n)$. Both $\mathcal{R}_n$ and $\mathcal{L}_n$ are increasing with respect to $\bar{g}$, which makes finding their
437   roots numerically straightforward.

438   Figure 12 shows the period $P_n(\bar{g})$ as predicted by the fixed points of Π_n (eq. (47)) plotted on their
439   respective intervals $\bar{g} \in [\bar{g}_+(n), \bar{g}_-(n)]$ (blue), as well as the cycle period acquired from numerical
440   integration of the full system of ODEs (orange). Note that the width of $n-n$ branches decreases with
441   n, which confirms the inequality in eq. (55). That is, bursts with more spikes occur on increasingly
442   smaller intervals of $\bar{g}$, which can be interpreted as a lost of robustness with respect to the coupling
443   strength of long-cyclic solutions. We also note the occurrence of bi-stability between pairs of $n-n$
444   and $(n+1)-(n+1)$ branches, which also confirms our initial observation in eq. (54).

445   As previously observed in fig. 11B our maps prediction of the cycle period is accurate for $n > 1$.
446   Recall that our reduction assumptions required a sufficiently large coupling strength, which we
447   numerically estimated to be $\bar{g} \approx 0.592\mathrm{mS/cm}^2$ in fig. 6. The mismatch in period for $1-1$ solutions,
448   but also the mismatch in the left bifurcation border $\bar{g}_-(n = 2)$ of the $2-2$ solution can be attributed
449   to the violation of that assumption. However, even for branches of large $n-n$ solutions there is
450   a mismatch between the bifurcation borders. Presumably our assumptions on the time scales of
451   w and s dynamics do not hold here, and can only be captured by more complex approximations.
452   Nevertheless, our map allows approximate extrapolation of the cycle period and the respective
453   bifurcation borders where numerical integration of the ODEs would require a very small time step.

4   DISCUSSION

454   Synaptic depression of inhibition is believed to play an important role in the generation of rhythmic
455   activity involved in many motor rhythms such as in leech swimming [24] and leech heart beat [25],
456   and in the lobster pyloric system [1, 2]. In inhibitory half-centre CPGs, such as believed to be
457   found in the struggling network of Xenopus tapdoles, synaptic depression can act as a burst
458   termination mechanism, enabling the alternation of bursting between the two sides of the CPG [11].
459   Mathematical modelling can shed light on the underlying mechanisms that enable the generation
460   of such anti-phase bursts, and help identify the components that control this rhythm allowing it to
461   switch between different patterns.

462   To study the mechanisms of burst generation in half-centre CPGs we have analysed a neuronal
463   model network that consists of a pair of inhibitory neurons that undergo a frequency dependent
464   synaptic depression. When the strength of synaptic inhibition between the neurons is varied, such
465   a simple network can display a range of different $n-n$ burst patterns. Using the timescale disparity
466   between neuronal and synaptic dynamics, we have reduced the network model of eight ODEs to a
467   scalar first return map Π_n of the slow depression variable d. This map Π_n is a composition of two
468   maps, F_n and Q_n, that model the evolution of the depression during the free and quiet phases of
469    $n-n$ solutions respectively. Both F_n and Q_n maps are constructed by using the dynamics of single
470   uncoupled neurons. Fixed points of Π_n are created in pairs through a fold bifurcation of maps,
471   where the stable fixed point correspond to stable $n-n$ burst solutions of the full two-cell system
472   of ODEs. The results from our one-dimensional map match excellently with numerical simulation
473   of the full network. Our results are in line with Brown's 1911 rhythmogenesis hypothesis, namely
474   that synaptic depression of inhibition is a mechanism by which anti-phase bursting may arise.

475   We have studied $n-n$ solutions assuming that the synaptic coupling $\bar{g}$ between the two cells
476   is symmetrical. However, Bose and Booth [6] have shown that asymmetrical coupling $(\bar{g}_1, \bar{g}_2)$ can
477   result in network solutions of type $m-n$, where one cell fires m spikes, while the other n spikes.
478   It is conceivable that our map construction can be extended to also capture such $m-n$ solutions.
479   Remember, in the case of symmetrical coupling with $n-n$ solutions, the timecourse of the depression
480   variables d_1 and d_2 were in anti-phase, and it was therefore sufficient to track only one of the two
481   variables. To capture the full network dynamics in case of asymmetrical coupling one would also
482   have to account for burst patterns of type $m-n$, where the solutions of the depression variables
483   d_1 and d_2 are not simply time-shifted versions of each other. To do that, one could track the state
484   of both variables by constructing a two-dimensional Poincaré map $\Pi(d_1, d_2)$. While geometrical
485   interpretation of two-dimensional maps remains challenging, there exist a number of recent studies
486   which have employed novel geometrical analysis methods to understand the dynamics of two-
487   dimensional maps of small neuronal networks [26, 27, 28]. Generally speaking, our map construction
488   approach is applicable to any small network, even with more than two neurons. As long as the

network dynamics occur on separable timescales the main challenges to the map construction lie in identifying the slowest variables, and finding an appropriate, simplified description of their respective timecourses. In theory, the reduction approach can be also applied to neuronal systems with more than two timescales [e.g. see 29].

In tadpoles, struggling is believed to be initiated by an increase in the firing frequency of reciprocally inhibitory commisural interneurons, which has been hypothesised to lead to stronger synaptic depression of inhibition and result in the iconic anti-phase bursting [11]. It would therefore be interesting to study how varying the cell intrinsic firing period T could affect the network rhythm. While we have laid out the framework to perform such an investigation, due to the choice of neural model we have avoided varying T. Recall that T is a derived parameter in the Morris and Lecar [12] model, and can therefore not be varied in isolation of other model parameters. This makes verifying any analytical results from our map analysis via numerical integration of the ODEs difficult. A more abstract model such as the quadratic integrate-and-fire model [30] allows varying T independently of other model parameters, and could be more fitting in this scenario.

Our simulations of the network showed that $n - n$ solutions lose robustness as their period is increased. That is, solutions with a larger cycle period occur on increasingly smaller intervals of the coupling strength. We were able to replicate this finding by numerically finding the respective left and right borders of stable $n - n$ branches of fixed points of Π_n, and showing that the distance between these borders shrinks with n. We have also noted the resemblance of our bifurcation diagram to one where such $n - n$ branches are created via a period-increment bifurcation with co-existent attractors of scalar linear maps with a discontinuity [31, 23]. It is worthwhile noting that the bifurcations of piecewise linear maps studied by Avrutin et al. and colleagues result from a "reinjection" mechanism, first described by Perez [32]. Here the orbit of a map performs multiple iterations on one side of the discontinuity, before jumping to the other side and being reinjected back into the initial side of the discontinuity. The stark difference of such a map to our map is that reinjection allows a single scalar map to produce periodic solutions of varying periods. In contrast, we rely on n different maps Π_n to describe the burst dynamics without explicitly capturing the period increment bifurcations. It is therefore conceivable that despite the complexity and non-linearity of the dynamics of our two-cell network, a single piecewise-linear map might be already sufficient to capture the mechanisms that shape the parameter space of the full system. In their discussion, Bose and Booth [6] briefly outline ideas about how such a linear map could be constructed.

In addition to stable $n - n$ solutions, the numerical continuation by Bose and Booth [6] also revealed branches of unstable $n - n$ solutions. While we have identified fold bifurcations of our burst map, we have not found corresponding bifurcations of the flow ODE system, and have generally ignored the significance of unstable map fixed points. However, the quadratic nature of the period bifurcation curve is reminiscent of a saddle-node on an invariance circle (SNIC) bifurcation, where the oscillation period lengthens and finally becomes infinite as a limit cycle coalesces with a saddle point. SNIC bifurcations have been studied in great detail [e.g. 33], and a next step would be to provide a rigorous explanation of not only the map dynamics, but also of the flow dynamics of the ODE system.

We have shown that when the strength of the maximum synaptic conductance is varied, synaptic depression of inhibition can enable our two-cell network to produce burst solutions of different periods. This result is in line with the idea that one role of synaptic depression in the nervous system may be to allow a finite size neuronal network to participate in different tasks by producing a large number of rhythms [6, 34, 11]. To change from one rhythm to another would only require a reconfiguration of the network through changes in synaptic coupling strength, which can occur through the process of learning. Thus short-term synaptic depression of inhibition may provide means for a network to adapt to environmental challenges without changing its topology, that is without the introduction or removal of neurons.

CONFLICT OF INTEREST STATEMENT

AUTHOR CONTRIBUTIONS

MO and CH contributed to conception and design of the study. MO performed numerical computation and analysis. All authors contributed to manuscript writing and revision.

FUNDING

ACKNOWLEDGEMENTS

DATA AVAILABILITY STATEMENT

The datasets generated for this study are available on request to the corresponding author.

REFERENCES

[1] Manor Y, Nadim F, Abbott L, Marder E. Temporal dynamics of graded synaptic transmission in the lobster stomatogastric ganglion. Journal of Neuroscience 17 (1997) 5610–5621. doi:10.1523/JNEUROSCI.17-14-05610.1997.

[2] Rabbah P, Nadim F. Distinct synaptic dynamics of heterogeneous pacemaker neurons in an oscillatory network. Journal of neurophysiology 97 (2007) 2239–2253. doi:10.1152/jn.01161.2006.

[3] Donovan M, Wenner P, Chub N, Tabak J, Rinzel J. Mechanisms of spontaneous activity in the developing spinal cord and their relevance to locomotion. Annals of the New York Academy of Sciences 860 (1998) 130–141.

[4] Nadim F, Manor Y. The role of short-term synaptic dynamics in motor control. Current Opinion in Neurobiology 10 (2000) 683–690. doi:10.1016/S0959-4388(00)00159-8.

[5] Nadim F, Manor Y, Kopell N, Marder E. Synaptic depression creates a switch that controls the frequency of an oscillatory circuit. Proceedings of the National Academy of Sciences 96 (1999) 8206–8211. doi:10.1073/pnas.96.14.8206.

[6] Bose A, Booth V. Co-existent activity patterns in inhibitory neuronal networks with short-term synaptic depression. Journal of Theoretical Biology 272 (2011) 42–54. doi:10.1016/j.jtbi.2010.12.001.

[7] Brown TG. The intrinsic factors in the act of progression in the mammal. Proceedings of the Royal Society of London. Series B 84 (1911) 308–319.

[8] Reiss RF. A theory and simulation of rhythmic behavior due to reciprocal inhibition in small nerve nets. Proceedings of the May 1-3, 1962, spring joint computer conference (ACM) (1962), 171–194. doi:10.1145/1460833.1460854.

[9] Perkel DH, Mulloney B. Motor pattern production in reciprocally inhibitory neurons exhibiting postinhibitory rebound. Science 185 (1974) 181–183. doi:10.1126/science.185.4146.181.

[10] Friesen WO. Reciprocal inhibition: a mechanism underlying oscillatory animal movements. Neuroscience & Biobehavioral Reviews 18 (1994) 547–553. doi:10.1016/0149-7634(94)90010-8.

[11] Li WC, Sautois B, Roberts A, Soffe SR. Reconfiguration of a vertebrate motor network: specific neuron recruitment and context-dependent synaptic plasticity. The Journal of Neuroscience 27 (2007) 12267–12276. doi:10.1523/JNEUROSCI.3694-07.2007.

[12] Morris C, Lecar H. Voltage oscillations in the barnacle giant muscle fiber. Biophysical Journal 35 (1981) 193–213. doi:10.1016/S0006-3495(81)84782-0.

[13] Matveev V, Bose A, Nadim F. Capturing the bursting dynamics of a two-cell inhibitory network using a one-dimensional map. Journal of Computational Neuroscience 23 (2007) 169–187. doi:10.1007/s10827-007-0026-x.

[14] Bose A, Manor Y, Nadim F. Bistable oscillations arising from synaptic depression. SIAM Journal on Applied Mathematics 62 (2001) 706–727. doi:10.1137/S0036139900378050.

[15] Tsodyks MV, Markram H. The neural code between neocortical pyramidal neurons depends on neurotransmitter release probability. Proceedings of the National Academy of Sciences 94 (1997) 719–723. doi:10.1073/pnas.94.2.719.

[16] Ermentrout GB, Terman DH. Mathematical foundations of neuroscience, Interdisciplinary Applied Mathematics, vol. 35 (Springer New York) (2010). doi:10.1007/978-0-387-87708-2.

[17] Ermentrout B. Simulating, analyzing, and animating dynamical systems: a guide to xppaut for researchers and students (SIAM) (2002).

[18] Virtanen P, Gommers R, Oliphant TE, Haberland M, Reddy T, Cournapeau D, et al. SciPy 1.0: Fundamental Algorithms for Scientific Computing in Python. Nature Methods 17 (2020) 261–272. doi:10.1038/s41592-019-0686-2.

[19] [Dataset] Olenik M. PyXPP. https://github.com/markolenik/PyXPP (2021).

[20] [Dataset] Gonzalez AS. pynverse. https://github.com/alvarosg/pynverse (2021).

[21] Gardini L, Avrutin V, Schanz M, Granados A, Sushko I. Organizing centers in parameter space of discontinuous 1d maps. the case of increasing/decreasing branches. ESAIM: Proceedings 36 (2012) 106–120. doi:10.1051/proc/201236009.

[22] Tramontana F, Gardini L, Avrutin V, Schanz M. Period adding in piecewise linear maps with two discontinuities. International Journal of Bifurcation and Chaos 22 (2012) 1250068. doi:10.1142/s021812741250068x.

[23] Avrutin V, Granados A, Schanz M. Sufficient conditions for a period incrementing big bang bifurcation in one-dimensional maps. Nonlinearity 24 (2011) 2575–2598. doi:10.1088/0951-7715/24/9/012.

[24] Mangan P, Cometa A, Friesen W. Modulation of swimming behavior in the medicinal leech. IV. Serotonin-induced alteration of synaptic interactions between neurons of the swim circuit. Journal of comparative physiology. A, Sensory, neural, and behavioral physiology 175 (1994) 723–736. doi:10.1007/BF00191844.

[25] Calabrese RL, Nadim F, Olsen ØH. Heartbeat control in the medicinal leech: A model system for understanding the origin, coordination, and modulation of rhythmic motor patterns. Journal of neurobiology 27 (1995) 390–402. doi:10.1002/neu.480270311.

[26] Akcay Z, Bose A, Nadim F. Effects of synaptic plasticity on phase and period locking in a network of two oscillatory neurons. The Journal of Mathematical Neuroscience 4 (2014) 8. doi:10.1186/2190-8567-4-8.

[27] Akcay Z, Huang X, Nadim F, Bose A. Phase-locking and bistability in neuronal networks with synaptic depression. Physica D: Nonlinear Phenomena 364 (2018) 8 – 21. doi:10.1016/j.physd. 2017.09.007.

[28] Liao G, Diekman C, Bose A. Entrainment Dynamics of Forced Hierarchical Circadian Systems Revealed by 2-Dimensional Maps. SIAM J. Appl. Dyn. Syst. (2020).

[29] Kuehn C. Multiple Time Scale Dynamics, Applied Mathematical Sciences, vol. 191 (Springer International Publishing) (2015). doi:10.1007/978-3-319-12316-5.

[30] Izhikevich EM. Which model to use for cortical spiking neurons? IEEE transactions on neural networks 15 (2004) 1063–1070. doi:10.1109/TNN.2004.832719.

[31] Avrutin V, Schanz M, Schenke B. Breaking the continuity of a piecewise linear map. ESAIM: Proceedings 36 (2012) 73–105. doi:10.1051/proc/201236008.

[32] Perez JM. Mechanism for global features of chaos in a driven nonlinear oscillator. Physical Review A 32 (1985) 2513–2516. doi:10.1103/physreva.32.2513.

630 [33] Ermentrout G, Kopell N. Parabolic bursting in an excitable System coupled with a slow
631   oscillation. SIAM Journal on Applied Mathematics 46 (1986) 233–253. doi:10.1137/0146017.
632 [34] Jalil S, Grigull J, Skinner FK. Novel bursting patterns emerging from model inhibitory networks
633   with synaptic depression. Journal of Computational Neuroscience 17 (2004) 31–45. doi:10.
634   1023/B:JCNS.0000023870.23322.0a.

FIGURE CAPTIONS

fig/nullclines-uncoupled.pdf

Figure 1. Periodic solution of relaxation-oscillator model neuron. **(A)** Projection of limit cycle onto (v, w)-phase plane with v-nullcline (blue, v_∞) and w-nullcline (orange, w_∞). Unstable fixed point p_f is indicated by an orange dot. **(B)** Corresponding voltage trace $v(t)$ of an action potential.

fig/depression-traces.pdf

Figure 2. Solution profiles of a $4 - 4$ burst. **(A)** Membrane potentials of cell 1 (v_1, blue), and cell 2 (v_2, orange). **(B)** Synaptic variables d_1 (blue) and s_1 (grey) of cell 1.

fig/burst-sols.pdf

Figure 3. Voltage traces of both cells of numerically stable solutions for increasing values of the coupling strength $\bar{g}$ (increasing top to bottom).
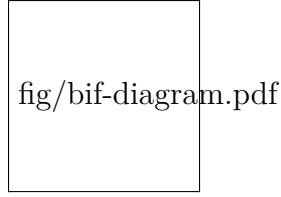
Figure 4. Numerically computed bifurcation diagrams of stable $n - n$ solutions for increasing coupling strength $\bar{g}$. **(A)** Period of stable solutions. Dashed lines show the interval between the $5-5$ and the suppressed solutions, where higher period $n-n$ solutions occur on increasingly smaller intervals of $\bar{g}$. **(B)** ISIs corresponding to $n - n$ solutions in (A). Long ISIs are associated with the quiet phase of a burst, short ISIs with the free phase. During the free phase, ISIs are of approximately constant duration T.
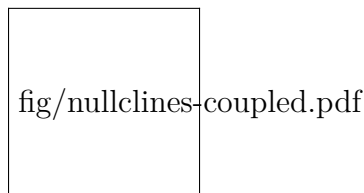
Figure 5. Nullclines v_∞ (blue) and w_∞ (orange) in the (v, w)-phase plane for different values of the total synaptic conductance $\bar{g}s$. For small $\bar{g}s < g^\star$, fixed point p_f is unstable (orange point). Larger values $\bar{g}s$ move v_∞ down in the (v, w)-plane until p_f changes stability (half orange, half blue point) at some critical total conductance value $\bar{g}s = g^\star$, and becomes stable (blue point) for $\bar{g} > g^\star$.
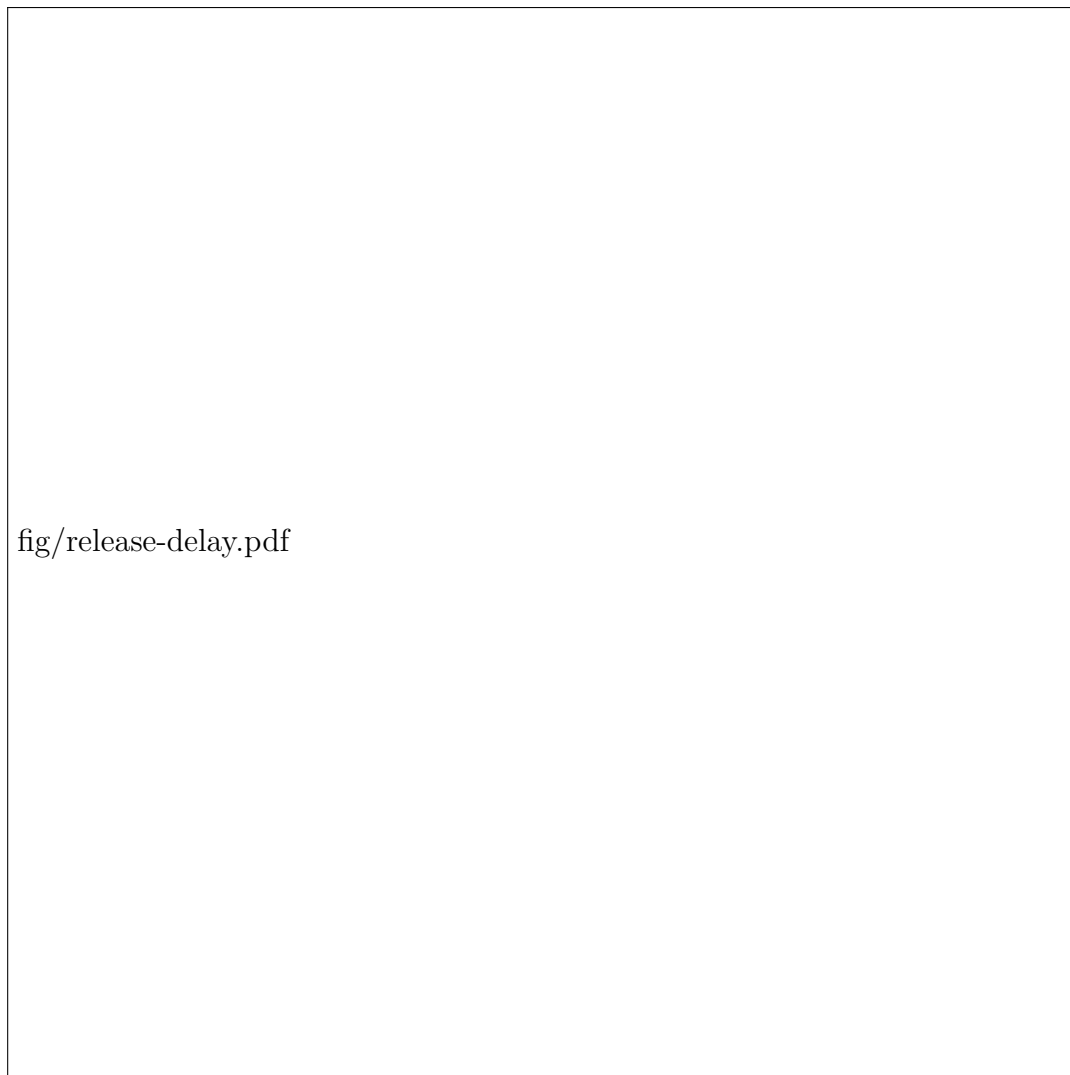
Figure 6. Numerically computed values of the release delay for varying $\bar{g}$. Each of the three branches (A, B, C) also shows the timecourse of the total synaptic conductance $\bar{g}s$ of a sample stable solution of both cells (blue and orange), as well as the release conductance $g^{\star}$ (dashed green line). **(A)** Branch corresponding to the $1 - 1$ solution. Here the quiet cell only spikes after a significant release delay. **(B)** Branch with a long release delay associated with a subset of $2 - 2$ solutions. Here the release condition is briefly satisfied after the first spike of cell 1. This does not cause firing of cell 2, which only occurs after the second spike of cell 1. **(C)** Branch with $n - n$ solutions where release delay is approximately zero and the release condition is sufficient for firing of cell 2.
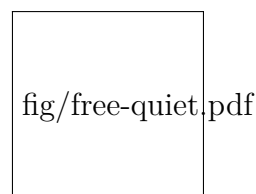
Figure 7. Schematic diagram of the free and quiet phases for a $3 - 3$ solution. **(A)** Membrane potentials of cell 1 (v_1) and cell 2 (v_2). The grey patches depict inter-burst-intervals Δt. **(B)** Total synaptic conductance of cell 1 ($\bar{g}s_1$) as it crosses the release conductance $g^{\star}$. **(C)** Solution $d_1(t)$ of depression variable of cell 1, during free (blue) and quiet phases (orange).
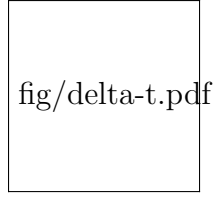
Figure 8. Numerically computed bifurcation diagram of Δt for varying $\bar{g}$. Each continuous branch is associated with a stable $n - n$ burst solution. Increasing $\bar{g}$ increases Δt until the solutions bifurcate at $\Delta t \approx T$.
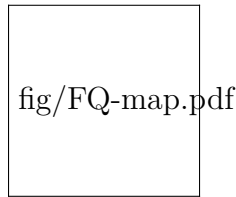

Figure 9. Maps F_n **(A)** and Q_n **(B)** for $\bar{g} = 0.6$ mS/cm^2 and $n = 1, 2, 3, 4$. Curves F_n intersect at d_s which is indicated by a dashed vertical line.
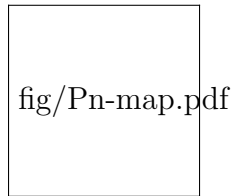

Figure 10. Map $\Pi_n : d^\star$. **(A)** Π_n for $n = 1, 2, 3, 4$ at $\bar{g} = 0.6$ mS/cm^2. **(B)** Π_2 with $n = 2$ for varying $\bar{g} \approx 0.01, 0.034, 0.3$ mS/cm^2. The identity function is illustrated by a diagonal line.
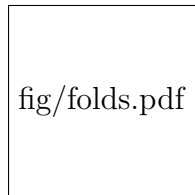

Figure 11. **(A)** Fold bifurcation diagrams of stable (continuous curves) and unstable (dotted curves) fixed points of Π_n for varying n. **(B)** Cycle periods computed from stable fixed points (blue), and the corresponding solution period from numerical integration of the system of ODEs (orange).
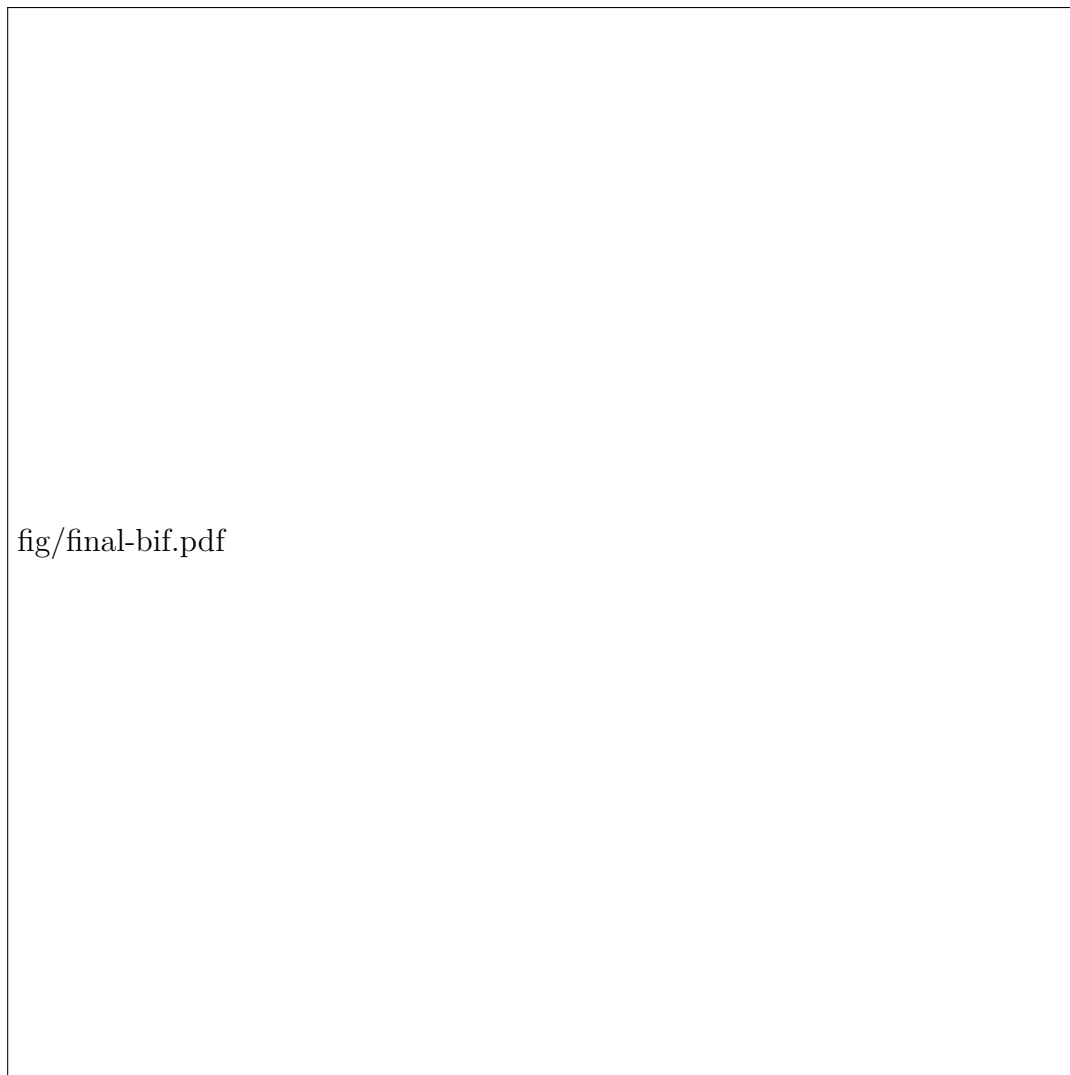
Figure 12. Bifurcation diagrams of stable $n - n$ solutions computed analytically from fixed points of Π_n and plotted on the respective intervals of $\bar{g} \in \left[\bar{g}_+(n), \bar{g}_-(n)\right]$ (blue), and computed from numerical integrations of the ODEs (orange).